

# Numerical Investigation of the Energetic-Exergetic Quasi-dynamic Performance of Mini-channel Solar Air Heaters

Ahmed Aboulmagd<sup>\*,\*\*†</sup> , Hesham Othman<sup>\*,\*\*\*</sup> , Ahmed ElDegwy<sup>\*,\*\*\*\*</sup> 

\*Mechanical Power Engineering Department, Faculty of Engineering, Cairo University, Giza 12613, Egypt.

\*\*Renewable Energy Department, Faculty of Energy and Environmental Engineering, The British University in Egypt, Shorouk 11837, Egypt.

\*\*\*Department of Mechanical Engineering, College of Engineering, Qassim University, Qassim 51452, Kingdom of Saudi Arabia.

\*\*\*\*Mechanical Engineering Department, Faculty of Engineering, Ahram Canadian University, Giza 12451, Egypt.

(a.aboulmagd@eng.cu.edu.eg, hothman@qec.edu.sa, mpdfoccu\_ahmed@cu.edu.eg)

†Corresponding Author; Ahmed Aboulmagd, a.aboulmagd@eng.cu.edu.eg

*Received: 16.09.2022 Accepted: 30.10.2022*

**Abstract-** Mini-channel solar air heaters (SAHs) are good candidates for implementation in hot air production fields due to their simple design, favourable performance and operational characteristics. In this paper, a numerical investigation of the energetic-exergetic performance of various mini-channel SAH absorber configurations is introduced using 3D CFD (computational fluid dynamics) analysis and under quasi-dynamic conditions. Three glass-covered mini-channel SAH absorber designs were investigated: a flat absorber with rectangular channels (RSAH), a tubular-channel absorber (TSAH) and a V-corrugated triangular channel absorber (VSAH). The performance analysis results are obtained and compared for all absorber configurations, including the simple, single-channel type solar air heater (SSAH). The developed CFD collector model was validated against available experimental data for the tubular mini-channel geometry. Hourly solar radiation values were calculated and meteorological data for Cairo, Egypt were obtained and coupled to the CFD model, based on typical seasonal days of the year. To highlight the absorber configuration of the best thermo-hydraulic performance, an energetic and exergetic performance analysis was performed. The maximum accumulative useful heat energy was achieved by the VSAH collector with average yearly increases of 79.42%, 6.42% and 29.69% as compared to SSAH, RSAH and TSAH, respectively. In addition, the average seasonal daily efficiency range for this type of collectors is 34.10%-41.32% as compared to 19.08%-22.78% for the SSAH type with an average increase of 79.73%. The average seasonal daily exergy efficiency range for this type of collectors is 1.60%-2.25% as compared to 0.49%-0.68% for the SSAH type with an average increase of 229.59%. Among all mini-channel collector configurations, VSAH collectors recorded the maximum collected annual energy of 1183.3 kWh/m<sup>2</sup>/y with an increase of 79.42% as compared to collected annual energy using SSAH collectors.

**Keywords** Solar air heater, mini-channel, energy, exergy, performance.

## 1. Introduction

Solar energy conversion is widely studied by researchers, over other renewable technologies since it is unrestricted and free on all surfaces of the entire earth [1]. In addition, industrialists are concerned about the depletion of

fossil fuels, increase in prices, and the harm that fossil fuel consumption does to the environment [2]. There are major benefits to using solar energy directly as useable energy in the form of heat [3]. There are several renewable heating supply technologies available on the market to meet the

increasing demand for thermal energy, such as flat solar thermal collectors and geothermal heat pumps [4].

Solar air heaters represent an attractive solar energy conversion equipment for solar system designers due to their simple structure, low-maintenance and reliable operation, especially under sunny climatic conditions. However, cost-effective and easy-to-manufacture products are not yet widespread. There are two main types of simple air heater collectors: the one-pass type with a single-cover or a double-cover and the two-pass type. For the first type with a single see-through cover plate, the air duct is the space separating the cover and the absorber sheet. If double covers are used, a sealed air gap separates the two see-through covers to reduce convective heat exchange, and the air duct is above the collector plate and below the covers. The second type uses either a divided air stream or takes the air flow through the outer section as a preheater before passing through the inner air duct [5].

Systems that utilize solar air heating consist of a network of interconnected solar thermal collectors that can be series-joined, parallel-joined, or joined as a combination of series and parallel modules. The majority of systems use a one-pass forced flow of air through the collector array with ambient air inlet to the system and solar-heated air output to the thermal load. [6]. Solar air systems have found use in single and multifamily residences, institutional buildings, sports facilities and industrial buildings. The reasons for this widespread use are that air is a reliable and economical heat carrier for heating a building space, ventilation air or even domestic hot water in summer [7]. They are advantageous over solar water heating systems in the aspects of simple fluid conduit works, no serious leakage problems, no corrosion or stagnation problems, rapid thermal response, and improved control. Applications in which solar air heaters are good choice include winter air conditioning and drying. In some cases, combined solar air and water heating installations can exist. Solar air heaters are also efficient and cost-effective as integrated with building skin. On the other side, there are some factors that limit the use of solar air heaters such as poor heat capacity of air which requires larger duct cross-sections and potential noise problems.

There are considerable experimental and numerical research concerning the design and thermal performance analysis of forced flow flat type solar air heaters in the literature [8]. The focus mainly is to enhance the conversion efficiency of the heater absorber module by suggesting different geometrical and flow configurations. Research efforts on the thermal performance enhancement of different configurations of solar air heaters are continuously developed. Aldabbagh et al. [9] have experimentally investigated single-pass and double-pass types of solar air heaters with layers of steel wire matrix in terms of thermal performance, taking into considerations the influence of varying mass flow rate on exit air temperature and collector efficiency. Keeping the mass flow rate constant, they discovered that multiple-pass solar air heaters offer better efficiency. In addition, a substantial increase in thermal efficiency was attained by using packed-bed collectors, compared to conventional ones. The finned-plate type of

solar air heater with double-pass flow has been the subject of the analytical and experimental study by El-Sebaei et al [10]. The finned-plate double pass and the v-corrugated-plate solar air heaters were compared in terms of performance. The influence of varying mass flow rates on the pressure drop and the thermal efficiency of the studied solar air heaters were also investigated. In comparison to the finned-plate double pass solar air heater, their findings indicated that the efficiency of the double pass v-corrugated-plate solar air heater increased by up to about 12%.

Ho et al. [11] investigated experimentally and theoretically a solar air heater design with double-pass, fins and baffles to study the effect of recirculation on its performance. The results of the performance comparison of different solar air heater designs proposed the double-pass device to improve the convection heat transfer coefficient and amplify the surface area of heat transfer. Based on their findings, the double-pass fined and baffled with recirculation design outperforms the other designs in terms of collector efficiency for a variety of reflux fractions and mass flow rates. Siddhartha et. al. [12] have developed a numerical particle swarm optimization algorithm to optimize the design and operation of a smooth flat absorber solar air heater and compared the model accuracy against experimental data. Yadav and Bhagoria [13] utilized a 2D CFD technique to introduce a study of the thermal and hydraulic flow characteristics in a synthetically roughened type of solar air heater. The results showed that the narrow diameter of the transverse wire ribs caused turbulence, which increased heat transfer over the duct. But using artificial roughness causes more friction losses.

Experimental research was done by Nowzari et al. [14] to determine the thermal characteristics of single and double-pass solar air collectors with standard glazing and quarter-holed tops. They found that for the same air mass flow rate, the efficiency of the double-pass type solar air heater consistently 5 to 23% more than that of the single pass air heater. A solar air heater of different configurations, e.g. single-pass and double-pass types with regular and punched covers and wire mesh slaps in place of an absorber sheet, was put through an experimental study by Nowzari et al. [15]. The recommended design for achieving the best thermal efficiency was a double-pass solar air heater with a quarter-punched top, a 3 cm hole interspacing at a value of 0.032 kg s<sup>-1</sup> for the mass flow rate. Dissa et al. [16] designed and experimented a compound absorber type of a solar air heater. By taking into account the impacts of heat capacity in each of its parts, the collector was modelled in an unsteady condition. The results indicated that during solar noon, the collector's thermal efficiency was about 61%, with 77, 142, 107, and 73 °C peak temperatures for the top cover, non-permeable and permeable solar absorbers, as well as air flow, respectively.

Singh et al. [17] presented a 2D CFD model for the investigation of the thermo-hydraulic characteristics of synthetically coarsened absorber type of a solar air heater with novel hyperbolic ribs. In their research, the roughness height was varied, and simulation runs were used to improve the rib profile parameters. It was discovered that rib

performance was best at 1 mm of roughness height, 10 mm of pitch, and 6000 Reynolds. Singh et. al [18] introduced an experimental and CFD comparative analysis of two novel ribs arrangement for performance enhancement in SAHs with average deviations values for the Nusselt number and friction coefficient within 6%. Their investigation incorporated rib parameters for the two setups and examined with six steps of Reynolds number in the range of 3000 to 18,000. Chamoli et. al [19] performed a numerical analysis for the thermo-hydraulic performance characterization of a SAH with winglet-embedded absorber with varying angle of attack as well as the Reynolds number. They discussed the effect of winglet vortex generator on various performance parameters, e.g. friction coefficient and Nusselt number. As concluded from their results, optimal winglet geometry and angle of attack were selected for the best heat transfer enhancement. Promthaisong et. al [20] evaluated the thermal performance of a SAH absorber with a wavy-triangular ribs. A parametric analysis was conducted to study the effect of Reynolds number blockage and pitch ratios on the key performance parameters. Hassan et al. [21] experimentally examined the performance of a tubular SAH (a cross-section of adjacent tubes along the air flow direction) as compared to the simple flat absorber SAH at different mass flow rates. Their results revealed higher efficiency and reduced top heat loss coefficient of the tubular design for the specified operating conditions.

Modern cultures depend heavily on energy. Entropy production and environmental impacts, however, are expenses related to energy conversion [22]. Saravanakumara et al. [23] conducted an exergy analysis of a curved SAH with artificial roughness ribs. A genetic-based parametric optimization of key design and operating variables were conducted. Singh et al. [24] employed a new concept by inserting rotating circular ribs in the air flow stream below the absorber plate of the SAH through a CFD study. The effects of different parameters on e.g. roughness size and pitch as well as the ribs rotational speed were included. Kumar et al. [25] performed an energetic and exergetic analysis to estimate the thermal performance of a SAH with winglet type artificial roughness on its absorber plate. A parametric study was conducted to obtain optimal setting for geometrical values of the roughness element.

Nidhul et al. [26] performed a critical review for ribbed SAH as well as 3D CFD performance analysis estimation of various V-rib absorber structures. They presented different shapes and designs of the ribs including crosswise, inclined, continuous and isolated patterns. They concluded that considerable improvement of heat transfer was attained with benefits not great enough to outweigh the pressure decrease. Beside the energy analysis, an exergetic analysis was also performed in their study to assess the various sorts of exergy destructions taking place in a SAH.

Compared to solar water heaters, SAH are more diverse, have more variable functioning, and are individually adapted to the user's requirements which raises doubts on the suitability of their standards [27]. According to the above literature review, more research and development efforts need to be exerted to promote the availability of efficient

designs and enhanced performance of solar air heaters. Current research efforts are directed to enhance SAH collector performance by inserting objects of different configurations to create artificial roughness, e.g. ribs on the absorber plate. Some works include novel concepts e.g. rotating turbulators and multi-effecting. However, among others, mini-channel solar air heaters of different geometrical configurations seem to be promising in terms of enhanced performance, simplicity and the ability to be standardized. The present work introduces a comparative design and energetic-exergetic performance analysis of three mini-channel absorber configurations of solar air heaters using a 3D CFD technique and under quasi-dynamic conditions with the aim of highlighting the configuration that having the best performance. The utilized mini-channel absorber configurations include rectangular, tubular and triangular cross-sections with the same hydraulic diameter. The results are also compared to those of the simple solar air heater configuration. The flow pattern within different mini-channel solar absorber configurations is introduced based on the local temperature and velocity contours to interpret the thermo-hydraulic performance of the solar air heater. To the authors' best knowledge, the introduced comparative quasi-dynamic based performance analysis of such type of mini-channel SAH using CFD was not covered in the related literature [28–30].

The aim of the present research is to conduct a numerical investigation of the thermo-hydraulic performance and flow patterns inside different mini-channel solar air heater absorber configurations, with the following specific objectives:

- Understand the fluid flow pattern inside different mini-channel solar air heater absorber configurations by studying temperature and velocity contours.
- Analyze the thermo-hydraulic performance parameters in terms of temperature layers within the solar air heater as well as the pressure drop across absorber channels.
- Perform a comparative energy and exergy performance analysis for various mini-channel solar air heaters and highlight designs with best energy and exergy records.

## 2. Materials and Methods

### 2.1. Solar Air Heater Configuration

The solar air heater under study is of the flat-plate single-pass type with different mini-channel absorber configurations. Solid models of the three mini-channel absorber configurations as well as the simple (single-channel) absorber are built for the CFD-based numerical study. A 3-mm thick single borosilicate glass cover separates the absorber top surface from the surrounding to reduce convection heat losses. The absorber plate-to-cover spacing is 3 cm. The external dimensions of the solar air heater are 1 m width by 1.5 m length by 0.08 m depth. A 5 cm layer of rockwool thermal insulation surrounds the bottom and sides of the solar absorber. The air passages to and from the inlet

and outlet headers are of circular cross-sections with 10 cm internal diameters. The 3D solid model and CFD numerical domain are developed within ANSYS-Fluent 2020 R2 platform [31]. Figure 1 shows the exterior 3D solid model of the SAH, including all components used in the computational field, including inlet and outlet header sections.

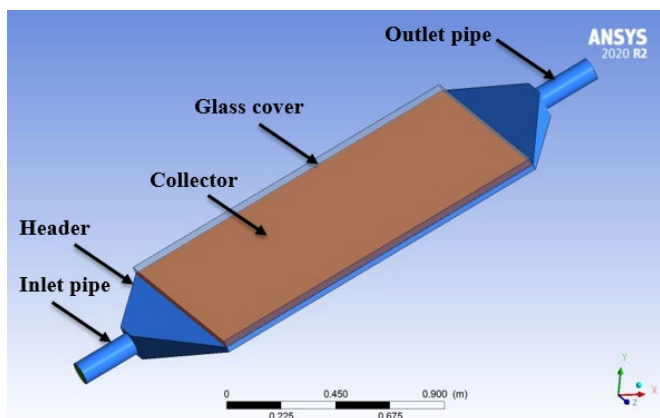


Fig. 1. The exterior 3D solid model of the studied SAH configurations.

Figure 2 shows the solar absorber geometrical designs used in the present study (simple SAH, rectangular, tubular and triangular mini-channel absorbers). The number of mini-channels for each absorber configuration is fixed along the aperture width. The hydraulic diameter is also fixed for all mini-channel types, in order to enable fair comparative analysis of the studied solar air heaters. The mini-channel characteristic dimension is 25 mm (internal) with 1 mm thickness and accordingly 37 mini-channels are used along the aperture width. The solar absorber channels are covered with a selective coating layer having an absorptivity value of 0.94 and an emissivity value of 0.05.

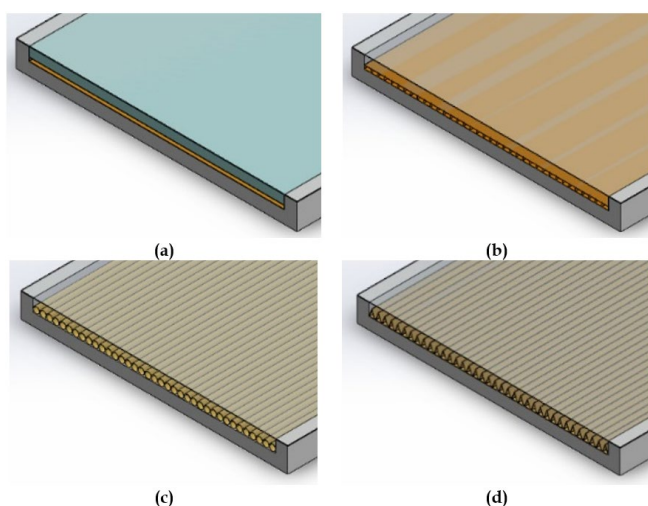


Fig. 2. SAH absorber configurations. (a) Simple absorber (b) Rectangular channel absorber. (c) Tubular channel absorber. (d) Triangular channel absorber.

Table 1 includes geometrical parameters and materials used for all absorber types of the solar air heater models. The collector azimuth angle is 0° and the tilt angle is 30°, based on optimized solar radiation collection.

## 2.2. CFD Model Development

The CFD model of mini-channel solar air heater configurations is created in ANSYS-Fluent 2020 R2 [31] using the finite volume method to resolve the flow problem. For connecting the velocity and pressure flow fields, the SIMPLE method was used. The 2<sup>nd</sup>-order upwind finite difference system was utilized for the discretization of convective terms, whereas the central difference finite difference scheme was used to handle diffusive terms. Iterations were stopped when the energy equation's relative error was less than 10<sup>-7</sup> and all other solved equations' relative errors were less than 10<sup>-4</sup>.

Table 1. Geometrical parameters and materials used for the solar air heater model.

Absorbing selective coating	Absorptivity [-]	0.94
	Emissivity [-]	0.05
Absorber (aluminium)	Hydraulic diameter [m]	0.025
	Length [m]	1.5
	Width [m]	1.0
	Absorber sheet thickness [m]	0.001
	Thermal conductivity [W/(m·K)]	220
	Number of mini-channels (rectangular, tubular and triangular)	37
	Thermal insulation (rockwool)	Insulation thickness [m]
	Thermal conductivity [W/(m·K)]	0.039 (at 25 °C)
	Density [kg/m <sup>3</sup> ]	160
	Specific heat capacity [J/kg.K]	1030
	Glass cover (borosilicate)	Number of glass covers
	Transmissivity of the glass cover [-]	0.92
	Emissivity of the glass cover [-]	0.88
	Thickness of glass [m]	0.003
	Thermal conductivity of glass [W/(m·K)]	1.2
	Absorber plate-to-cover spacing	0.03
Header sections	Inlet diameter [m]	0.1
	Outlet diameter [m]	0.1
Header sections	Azimuth angle [°]	0
	Tilt angle [°]	30

### 2.2.1. Operating and Boundary Conditions

Inside the mini-channels of different cross-sections, ambient air flows at an inlet temperature that corresponds to ambient air conditions of the specified seasonal day (between

15 and 40 °C). The mass flow rate per square meter of the collector aperture is set as 0.02 kg/(s·m<sup>2</sup>), as per guidelines of the European standard EN 12975-2:2006 for performance assessment of solar thermal systems [32]. Therefore, at the inlet to the collector, a uniform flow rate of 0.03 kg/s with a turbulence intensity of 5% is introduced. Figure 3 illustrates various boundary conditions imposed on the mathematical model of the solar air heater collector.

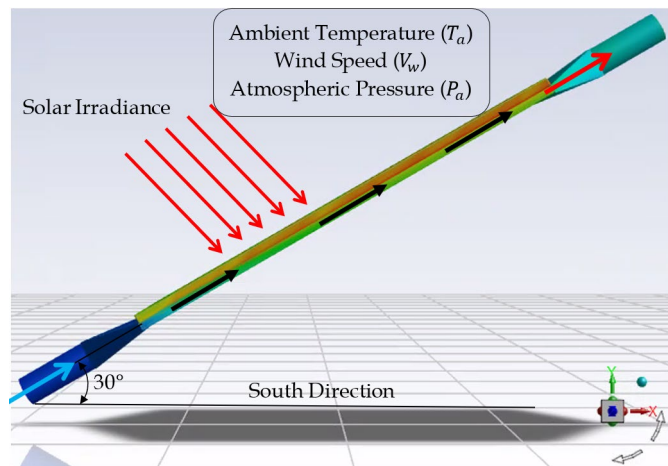


**Fig. 3.** Boundary conditions as imposed on the mathematical model of the SAH.

The internal channel surface is demonstrated as a no-slip boundary wall. Outside the computational domain, static atmospheric pressure was adopted. In order to evaluate top heat losses from the collector, ambient air temperature and wind speed are supplied to the computational field surrounding the collector on an hourly basis. The solar calculator within ANSYS software evaluates different components of solar irradiance on the collector plan (direct normal, diffuse and reflected solar irradiance) based on the specified latitude and longitude of the location as well as collector tilt and azimuth angles. The formulated boundary conditions are summarized in Table 2.

The following assumptions are made for the development of the mathematical model:

1. Quasi-dynamic conditions are to be applied over the entire time step and span (day length) for the calculations without loss of accuracy,
2. Optical properties of the materials used in the solar air heater are to be non-changing over the operating temperature range,
3. Incompressible flow of air within the channels, due to low flow velocities,
4. Isotropic diffuse model for the global solar irradiance on the tilted collector surface.

2.2.2. Mesh Generation and Model Validation

The computational field of the solar air collector is meshed with more than 4,450,000 tetrahedral finite volume cells. This type of mesh elements was selected to be used in the present study due to its suitability with complex geometries. A quality mesh is created using the surface

configuration that the design modeler developed and saved as a mesh file. ANSYS Fluent Solver is used to map the outcomes once the produced field matrix equations have been solved. Figure 4a shows the generated mesh for the collector domain.

**Table 2.** Summary of the used boundary conditions.

Surface	Boundary condition	Thermal condition	Solar boundary conditions
Solar field top side (glass)	Semi-transparent	Solar calculator	Absorptivity: Direct visible = 0.05, Direct IR = 0.05, Diffuse hemispherical = 0.05
Collector	Opaque and black body	Program calculator	Transitivity: Direct visible = 0.92, Direct IR = 0.92, Diffuse hemispherical = 0.92
Solar field sides	Opaque and black body	Program calculator	Internal emissivity = 0.8
Pipes and headers	Opaque and black body	Program calculator	Internal emissivity = 0.8
Back wall	Opaque and black body	Program calculator	Absorptivity: Internal emissivity = 0.8, Direct visible = 0.2, Direct IR = 0.2
Inlet boundary	Velocity	Constant temperature (T <sub>a</sub> )	Internal emissivity = 0.8
Outlet boundary	Constant pressure outlet	-----	Internal emissivity = 1

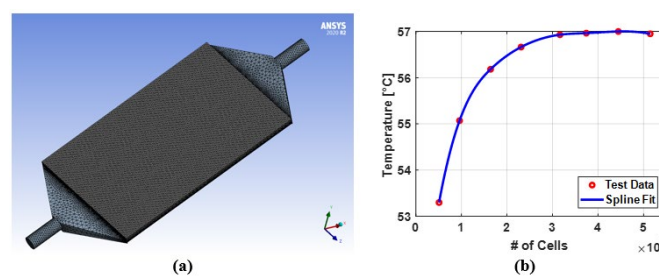


**Fig. 4.** (a) The generated mesh for the SAH collector computational domain. (b) Grid independence test results based on the outlet temperature.

The mesh dependency was studied by solving the flow domain for eight mesh structures made of 510,000 – 950,000 – 1,642,000 – 2,321,000 – 3,168,000 – 3,751,000 – 4,451,000 and 5,144,000 cells respectively. Figure 4b illustrates the results of the grid independence test for the rectangular mini-channel absorber at 12:00 pm on June 21. The outlet air temperature begins to stabilize at about 3,750,000 mesh elements. The results showed that there is a 7% difference in air outlet temperature between the coarser

and finer meshes, but only a 0.07% difference between the two finer ones. The coupled method chosen was pressure-velocity coupling, PRESTO was utilized for pressure interpolation, and 1<sup>st</sup>-order discretization techniques were employed for the viscous and convection elements of the governing equations. Utilizing the Green-Gauss node-based technique, gradients are calculated. The simulations were completed using the control volume approach in the ANSYS Fluent CFD engine. When the total residue showed no further decline with increasing the number of iterations, convergence had been thoroughly examined and the iterations were considered complete. Additionally, the scaled residuals for continuity, turbulent kinetic energy, turbulence dissipation rate, and momentum were roughly  $10^{-4}$ ,  $10^{-4}$ ,  $10^{-4}$ , and  $10^{-5}$ , respectively. The 3D CFD solution domains of the simple (single channel), rectangular, tubular and triangular channel absorbers of the SAH are obtained at each hourly time step starting 8:00 to 16:00 for the specified representative days from each season.

For the purpose of validation, the results of the developed CFD model are compared to those from the experimental work of Hassan et al. [21] under the same operating conditions. Figure 5 shows the validation results of the SAH model for the simple (SSAH) and tubular (TSAH) absorber geometries, on hourly-basis results and on average daily-basis. Three temperature levels within the SAH were used for model validation: outlet air temperature ( $T_{out}$ ), glass cover temperature ( $T_c$ ) and absorber temperature ( $T_p$ ).

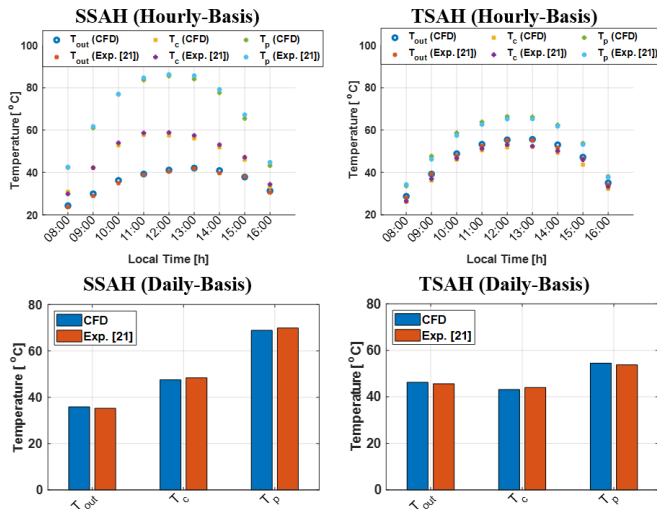


**Fig. 5.** Validation of the SAH model against experimental data from [21] for the simple flat and tubular absorber geometries.

A comparison between numerical CFD and experimental temperature profiles for flat and tubular types of the SAH showed that numerical CFD outputs fit well with experimental results which ensures the accuracy of the developed model. The maximum error in the case of flat SAH is around 3.5% and in the case of tubular SAH is around 5%.

2.3. Weather Data

Hourly meteorological parameters for the specified location (Cairo – Egypt: E 31° 00' 30", N 30° 02' 10") are based on the typical meteorological year (TMY) data file obtained from [33]. The data include ambient temperature ( $T_a$ ), wind speed ( $V_w$ ) and barometric pressure ( $P_a$ ). Four representative days of the year are selected as input to the numerical quasi-dynamic model to reflect seasonal variations: Mar. 20 (spring solstice), Jun. 21 (summer solstice), Sep. 23 (autumn solstice) and Dec. 22 (winter solstice). A time span of 8 hours, from 8:00 am to 4:00 pm is selected for the simulation of input/output parameters of the numerical model. Hourly variations of ambient air temperature, wind speed and atmospheric pressure around collector plane for the specified seasonal days at the selected location are shown in Fig. 6.

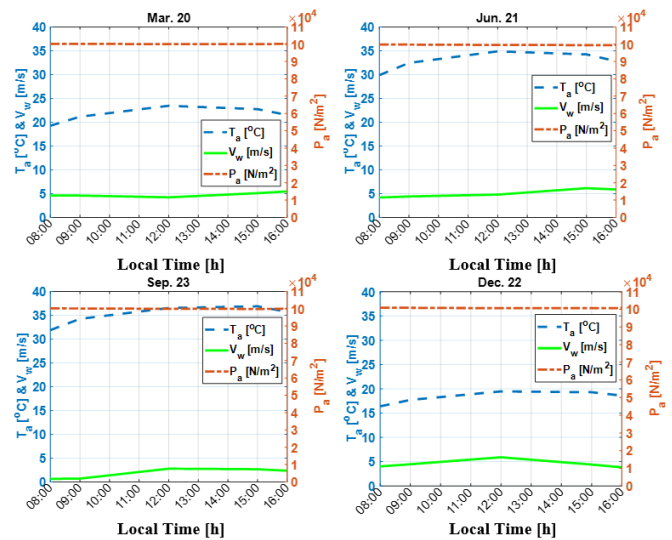


**Fig. 6.** Variations of ambient air temperature, wind speed and ambient pressure for representative seasonal days at the specified location.

Fundamental solar irradiance components: direct normal irradiance ( $DNI$ ), diffuse horizontal irradiance ( $DHI$ ) and global horizontal irradiance ( $GHI$ ) are obtained from ANSYS solar calculator on an hourly basis. The tilted global solar irradiance on the collector surface ( $G_T$ ) is then obtained and accordingly the amount of energy collected in kWh/m<sup>2</sup> of the collector aperture is calculated. Table 3 provides statistics for the daily collected energy on the collector plane, average ambient temperature and average wind speed on the specified seasonal days. The most effective parameter is the energy collected by a unit area of the collector aperture which has the highest records in June and September. In addition, the average ambient temperature is high in these two months, as compared to March and September. The wind speed affects the convective heat transfer coefficient from the collector top cover to the surrounding atmosphere. The highest record of this parameter is in June.

**Table 3:** Statistics of collected solar energy and meteorological data on the specified seasonal days.

Energy [kWh/m <sup>2</sup> ]	Average T <sub>a</sub> [°C]	Average V <sub>w</sub> [m/s]	Average P <sub>a</sub> [N/m <sup>2</sup> ]	Energy [kWh/m <sup>2</sup> ]
Mar. 20	5.82	22.09	4.68	100120.9
Jun. 21	6.87	33.40	5.06	99621.2
Sep. 23	6.17	35.48	2.00	99980.2
Dec. 22	3.81	18.60	4.81	100745.2

2.4. Governing Equations

The studied flow field is three-dimensional, compressible under quasi-dynamic conditions (with one hour time-step). Therefore, the required governing equations to numerically solve this flow field are the continuity, the momentum and the energy equations [34]. The continuity equation under quasi-steady conditions, without source term and assuming compressible flow is,

$$\frac{\partial(\rho v_i)}{\partial x_i} = 0 \tag{1}$$

where the flow velocity in the *i*<sup>th</sup>-direction is represented by *v<sub>i</sub>* and  $\rho$  is the fluid density.

The momentum equation is given by

$$\rho \frac{\partial(u_i u_j)}{\partial x_j} = -\frac{\partial P}{\partial x_i} + \mu \frac{\partial}{\partial x_j} \left[ \frac{\partial u_i}{\partial x_j} + \frac{\partial u_j}{\partial x_i} - \frac{2}{3} \delta_{ij} \frac{\partial u_i}{\partial x_j} \right] + \rho \frac{\partial}{\partial x_j} (-u_i' u_j') \tag{2}$$

where  $\mathbf{u}_j$  is the fluid velocity in the y-direction, *P* is the local pressure,  $\mu$  is the fluid dynamic viscosity,  $\mathbf{u}_j'$  is the fluctuated velocity,  $\mathbf{u}_i' \mathbf{u}_j'$  is the turbulent shear stress, and  $\delta_{ij}$  is the Kronecker delta (which equals 1.0, if *i* = *j*, or 0.0, if *i* ≠ *j*).

The energy equation is given by

$$\frac{\partial(\rho u_j E)}{\partial x_j} = -\frac{\partial(\rho u_j)}{\partial x_j} + \frac{\partial(u_j \tau_{ij})}{\partial x_i} + \frac{\partial}{\partial x_j} \left( k \frac{\partial T}{\partial x_j} \right) + S_E \tag{3}$$

with *E* is the total energy content in the fluid, given by

$$E = e + \frac{1}{2}(u^2 + v^2 + w^2) \tag{4}$$

where *e* is the specific energy content in the fluid (enthalpy).

The turbulence modeling approach in this work is the standard k-ε model, given by

$$\frac{\partial}{\partial x_i} (\rho k u_i) = \frac{\partial}{\partial x_j} \left[ \left( \mu + \frac{\mu_t}{\sigma_k} \right) \frac{\partial k}{\partial x_j} \right] + G_k + G_b - \rho \epsilon - Y_M + S_k \tag{5}$$

and

$$\frac{\partial}{\partial x_i} (\rho \epsilon u_i) = \frac{\partial}{\partial x_j} \left[ \left( \mu + \frac{\mu_t}{\sigma_\epsilon} \right) \frac{\partial \epsilon}{\partial x_j} \right] + G_{1\epsilon} \frac{\epsilon}{k} (G_k + C_{3\epsilon} G_b) - C_{2\epsilon} \rho \frac{\epsilon^2}{k} + S_\epsilon \tag{6}$$

where the coefficient *G<sub>k</sub>* describes how mean velocity gradients cause turbulence to produce kinetic energy. The buoyancy-induced creation of kinetic turbulence is denoted by the symbol *G<sub>b</sub>*. The variable dilatation in compressible turbulence's contribution to the total dissipation rate is represented by the symbol *Y<sub>M</sub>*. *C<sub>1ε</sub>*, *C<sub>2ε</sub>* and *C<sub>3ε</sub>* are constants. The turbulent Prandtl numbers for *k* and are, respectively,  $\sigma_k$  and  $\sigma_\epsilon$ . *S<sub>k</sub>* and *S<sub>ε</sub>* are the source terms.

The eddy viscosity,  $\mu_t$ , is calculated by merging *k* and  $\epsilon$  as

$$\mu_t = \rho C_\mu \frac{k^2}{\epsilon} \tag{7}$$

where *C<sub>μ</sub>* is a constant.

The default values of the model constants are *C<sub>1ε</sub>* = 1.44, *C<sub>2ε</sub>* = 1.92 and *C<sub>μ</sub>* = 0.09,  $\sigma_k$  = 1 and  $\sigma_\epsilon$  = 1.3.

These default settings were established by tests with basic turbulent shear flows, such as uniform shear flows and deteriorating isotropic grid turbulence, in both air and water. They have been discovered to function rather well for a variety of free and wall-bounded shear flows. The air properties are evaluated within ANSYS Fluent calculation platform as function of the fluid local temperature inside the mini-channel absorber. The discrete ordinates (DO) radiation model is used in this study due to its good functionality across full range of optical thicknesses with accurate results. According to the orientation of the solar air collector, the solar energy calculator has been used to determine direct and diffuse solar radiation for a specific time, date, and location. It also took into account opaque and semi-transparent mass media, such as the collector body surface and glass cover. The global solar irradiance on the tilted collector surface (*G<sub>T</sub>*) is obtained using the isotropic diffuse model [35], given by

$$G_T = DNI \cdot \cos \theta + DHI \frac{(1 + \cos \beta_c)}{2} + GHI \cdot R_g \frac{(1 - \cos \beta_c)}{2} \tag{8}$$

where *R<sub>g</sub>* is the reflectivity of the surrounding ground (selected as an average value of 0.5),  $\theta$  is the incidence angle of solar radiation on the collector surface and  $\beta_c$  is the collector tilt angle.

At the top collector cover, heat is being lost by convection and radiation. The wind heat transfer coefficient (*h<sub>w</sub>*) is calculated above the cover surface and to the surrounding ambient air, given by [35],

$$h_w = 5.7 + 3.8V_w \tag{9}$$

where *V<sub>w</sub>* is the hourly wind speed value.

The useful heat gain ( $\dot{q}_u$ ) of the SAH is given by

$$\dot{q}_u = \dot{m} c_p (T_{out} - T_{in}) \tag{10}$$

where  $\dot{m}$  is the air mass flow rate, *c<sub>p</sub>* is the mean specific heat of air, *T<sub>in</sub>* and *T<sub>out</sub>* are the inlet and outlet air temperatures, respectively.

The SAH collector efficiency ( $\eta_{coll}$ ) is given by

$$\eta_{coll} = \frac{\dot{q}_u}{G_T \cdot A_{ap}} \tag{11}$$

where *A<sub>ap</sub>* is the aperture area of the collector.

The accumulative useful heat energy (*Q<sub>u</sub>*) for each collector configuration is given by Eq. (12), obtained by integrating the useful heat gain from the collector over the specified time period.

$$Q_u = \int \dot{q}_u dt \tag{12}$$

The collector exergy efficiency is expressed as

$$\eta_{exer} = \frac{\psi_{rec}}{\psi_{exp}} \quad (13)$$

where  $\psi_{rec}$  is the recovered exergy stream for the working air and  $\psi_{exp}$  is the expended exergy stream by the solar irradiance on the collector aperture.

The recovered exergy stream is given by [36, 37]

$$\psi_{rec} = G_T A_{ap} \eta_{coll} \eta_C - \dot{W}(1 - \eta_C) \quad (14)$$

where  $\eta_C$  is Carnot efficiency and  $\dot{W}$  is the fan power. Carnot efficiency is a function of the ambient air temperature ( $T_a$ ) and the mean fluid temperature ( $T_{f,m}$ ) between the inlet and outlet sections, given by

$$\eta_C = 1 - \frac{T_a}{T_{f,m}} \quad (15)$$

The fan power is given by

$$\dot{W} = \frac{\Delta P \cdot \dot{V}}{\eta} \quad (16)$$

where  $\dot{V}$  is the air volume flow rate [m<sup>3</sup>/s], calculated based on the mean air density between the inlet and outlet sections and  $\eta$  is the combined efficiency of the fan and its drive motor, assumed to be 0.65.

The expended exergy stream by solar radiation is expressed as

$$\psi_{exp} = G_T \left( 1 - \frac{T_a}{T_s} \right) \quad (17)$$

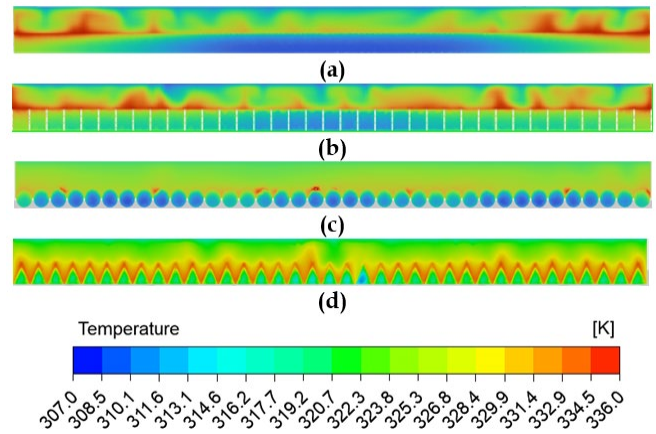
where  $T_s$  is the sun skin temperature, evaluated as 5762 K, assuming a black body behavior.

### 3. Results and Discussions

#### 3.1. Fluid Flow Pattern

To investigate the characteristics of the fluid flow pattern of different mini-channel absorber configurations, sample contour plots of the local temperature and the local velocity of the heated air within the collector are to be shown. Figure 7 shows sample temperature contours for different mini-channel absorber cross-sections, located midway along the flow direction, of the SAH at 12:00 pm on June 21. For the simple (single channel) solar air heater, higher air velocities are available within the core region which results in lower air temperatures. Higher temperatures are found near both sides of the air channel due to lower fluid velocities and higher effects of thermal boundary layers attached to the absorber plate. For the rectangular and tubular channel SAHs, higher fluid temperatures are achieved within the mini-channels due to larger heat transfer surface areas. The triangular absorber achieves the highest air temperature inside the mini-channels, with a higher degree of uniformity as compared to other absorber configurations. Higher absorber temperatures are achieved by the rectangular and triangular absorbers, as compared to those for the simple and tubular absorbers. It can be noticed that the fluid temperature within the external boundary layer of the triangular mini-channel absorber is uniform all over all mini-channels. In addition, this thermal boundary layer is thinner and concentrated around the mini-channels as compared to other mini-channel configurations, which creates a considerable thermal buffer within the

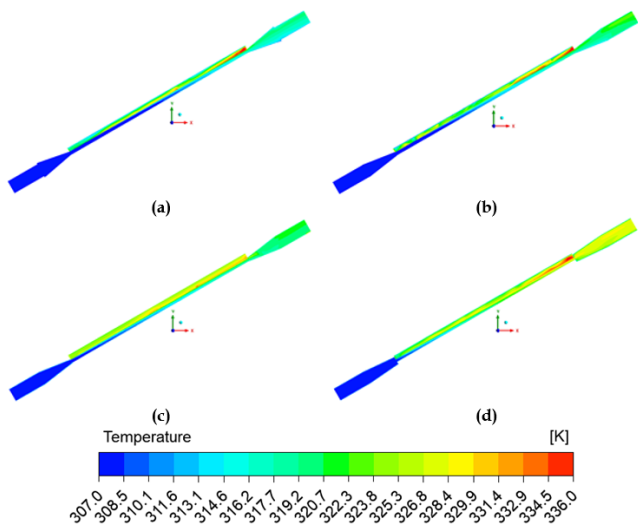
absorber-cover region and contributes to reducing the top losses.



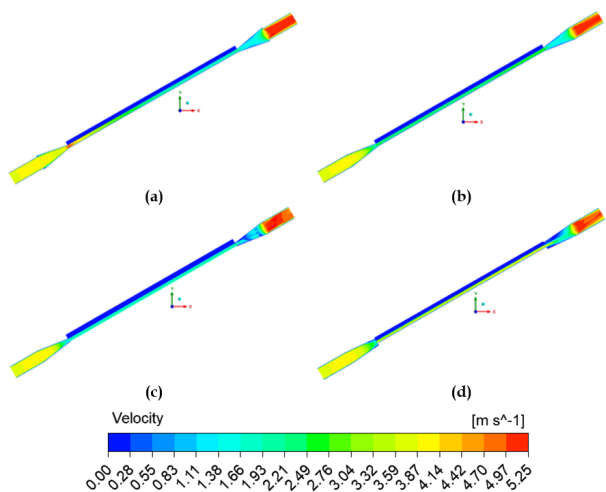
**Fig. 7.** Temperature contours for different mini-channel absorber cross-sections of the SAH (at 12:00 pm on June 21). (a) Simple, (b) Rectangular, (c) Tubular and (d) Triangular.

Figure 8 shows sample temperature contours in the longitudinal flow direction along different mini-channel absorber configurations of the SAH at 12:00 pm on June 21, located midway across the collector width. At the inlet to each SAH configuration, the inlet temperature is uniform within the header section which is the ambient air temperature. With uniform input incident solar radiation on the aperture surface, the fluid temperature is increased at different rates along the flow direction of each absorber configuration. For the simple absorber geometry, a relatively low temperature is found within the flow direction with relatively lower outlet temperature as compared to other configurations. Higher temperatures are achieved within the rectangular and tubular mini-channel geometries along the flow direction and accordingly higher outlet temperatures. For the triangular absorber configuration, the bulk fluid temperature starts to show higher values earlier within the mini-channel flow direction towards the outlet header and accordingly maximum outlet temperature is achieved.

Figure 9 shows sample velocity contours in the longitudinal flow direction along different mini-channel absorber configurations of the SAH at 12:00 pm on June 21, located midway across the collector width. The flow velocity is uniform at the inlet section of all absorber configurations and the velocity field is almost identical within all inlet headers. Recalling that the mass flow rate is constant through the collectors and following the ideal gas law, with heat being added to each collector absorber, the fluid density decreases and accordingly the flow velocity increases along the flow direction. At the outlet from mini-channels of all absorber configurations, the local flow velocities attain their maximum values as the collecting headers converge, especially within the centerline core regions of the outlet circular headers. As expected, lowest local flow velocities are found within the single channel absorber which leads to the lowest pressure drop among all absorber configurations. On the other side, the triangular absorber configuration achieved the highest local velocities among others which should raise the pressure drop across the collector flow.



**Fig. 8.** Temperature contours in the longitudinal flow direction along different mini-channel absorber configurations of the SAH (at 12:00 pm on June 21). (a) Simple, (b) Rectangular, (c) Tubular and (d) Triangular.



**Fig. 9.** Velocity contours in the longitudinal flow direction along different mini-channel absorber configurations of the SAH (at 12:00 pm on June 21). (a) Simple, (b) Rectangular, (c) Tubular and (d) Triangular absorber.

### 3.2. Thermo-hydraulic and Energy Performance Analysis

To perform the energy analysis of the collector, the thermo-hydraulic performance is introduced in terms of the temperature profile and pressure drop at various locations. The average hourly quasi-dynamic mean temperature data for different SAH absorber configurations are obtained from the CFD analysis for the selected representative days of the year. Simulation is performed from 8:00 to 16:00 (morning to afternoon) for each day.

For the specified input mass flow rate and inlet temperature stream ( $T_{in}$ ), hourly temperature profiles for outlet stream ( $T_{out}$ ) and absorber surface ( $T_p$ ) are investigated and the results are displayed in Fig. 10 and Fig. 11. As expected, maximum temperature was achieved around the solar noon for all absorber configurations on all seasonal

days. Simple SAH absorber achieved the lowest hourly temperature profile values among all other configurations with maximum absorber plate temperature of 60 °C and outlet temperature of 52 °C on Sep. 23. Rectangular and tubular absorber configurations have the highest absorber temperatures for all seasons. Triangular absorber configuration has achieved the highest maximum outlet temperature for all seasons. This is due to higher surface area exposed to solar radiation in case of triangular channels as compared to other configurations.

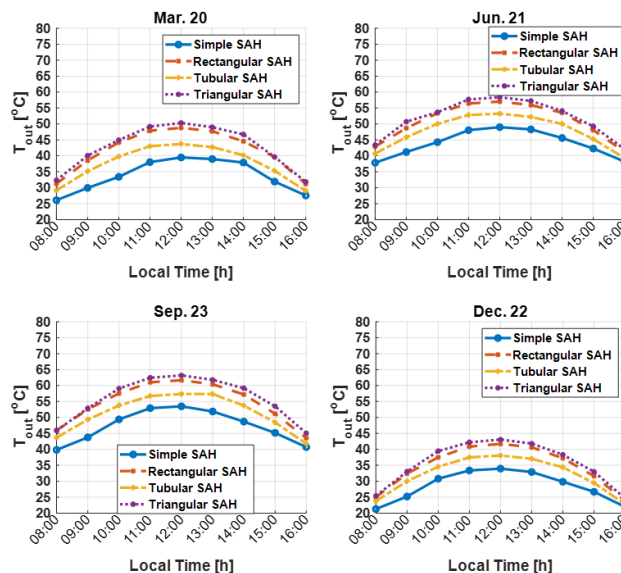


**Fig. 10.** Seasonal variations of the mean outlet temperature for different SAH absorber configurations).

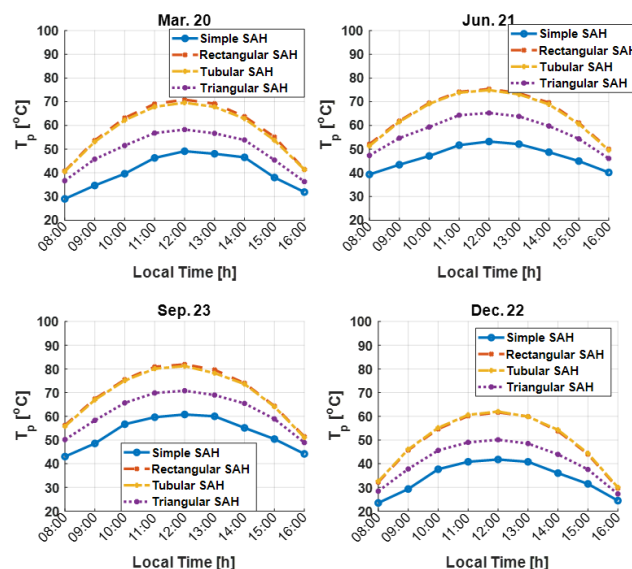


**Fig. 11.** Seasonal variations of the mean absorber temperature for different SAH absorber configurations).

Figure 12 shows the hourly variation of the pressure drop across the collector for the selected seasonal days of the year. It is obvious that simple solar air heaters have the lowest pressure drop values for all seasons, followed by tubular, rectangular and triangular absorber solar air heaters which have the highest pressure drop values. The maximum pressure drop values are associated with maximum operating

temperatures achieved at noon times for all types of collector absorbers. This is due to the reduction in fluid density with increased temperature at the outlet section of the collectors which results in lower outlet pressure. Maximum average pressure drops are associated with TSAH and VSAH collectors for all seasons as compared to SSAH and RSAH collectors due to higher flow velocities. For instance, the average increases in pressure drop are 49.17% and 25.80% for VSAH collectors as compared to SSAH and RSAH collectors, respectively.

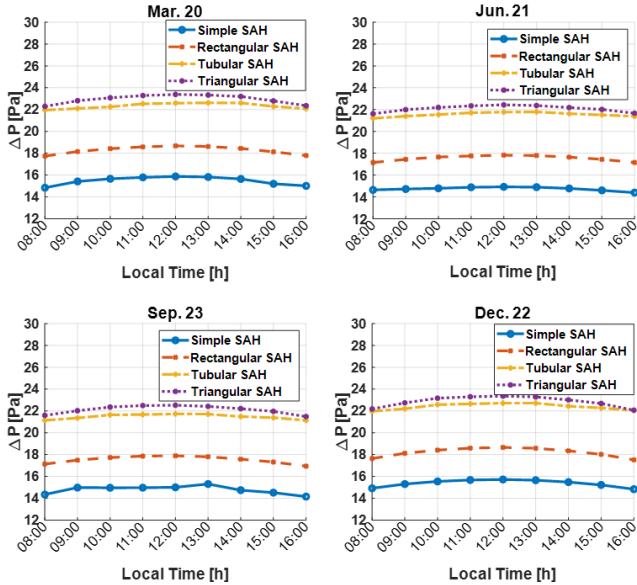


Fig. 12. Seasonal variations of pressure drop for different SAH absorber configurations.

Figure 13 through Figure 16 show the hourly variations of useful heat gain and collector efficiency as obtained from Eqs. (10) and (11), respectively for different SAH absorber configurations on a seasonal basis. The triangular SAH absorber has achieved maximum useful heat gain for all seasons thus having maximum instantaneous collector efficiency of 82.13%, 71.80%, 80.50% and 71.68% on Mar. 20, Jun. 21, Sept. 23 and Dec. 22, respectively. Over the operating temperature range of the SAH, the mean efficiency of the triangular absorber was 43.19% as compared to 41.03% and 34.59% for rectangular and tubular collector efficiencies.

Figure 17 shows the accumulative useful heat energy from each SAH absorber configuration for all seasons. It is obvious from the plot that triangular SAH absorbers have the highest accumulative heat energy on all representative seasonal days. The simulation results for accumulative heat energy reflect the results obtained from the simulated collector efficiency curves.

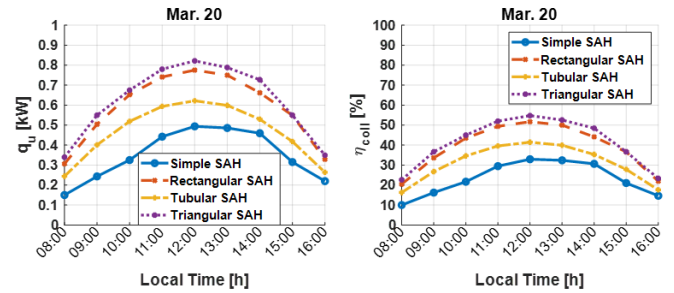


Fig. 13. Variations of useful heat gain (left) and collector efficiency (right) for different SAH absorber configurations on Mar. 20.

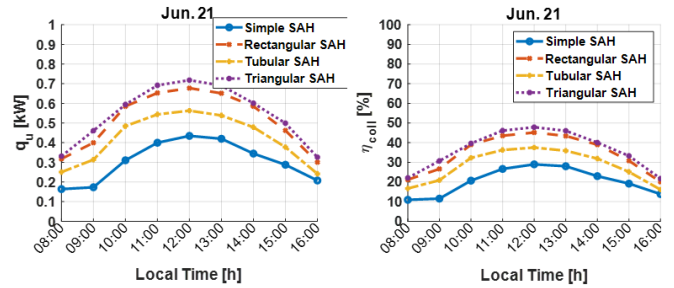


Fig. 14. Variations of useful heat gain (left) and collector efficiency (right) for different SAH absorber configurations on Jun. 21.

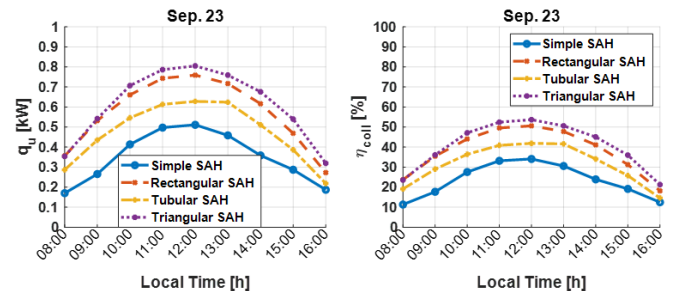


Fig. 15. Variations of useful heat gain (left) and collector efficiency (right) for different SAH absorber configurations on Sep. 23.

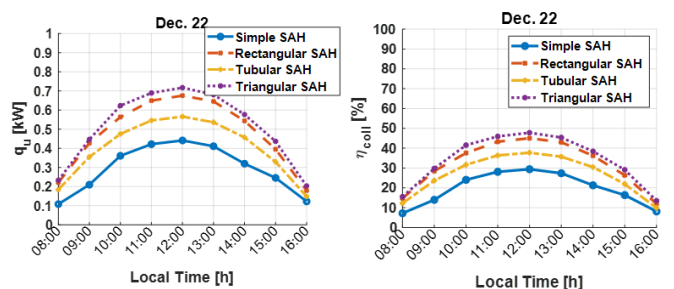
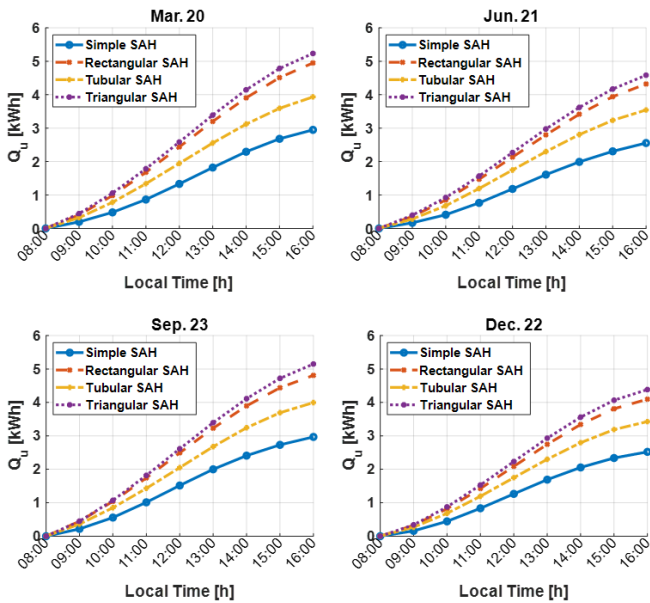


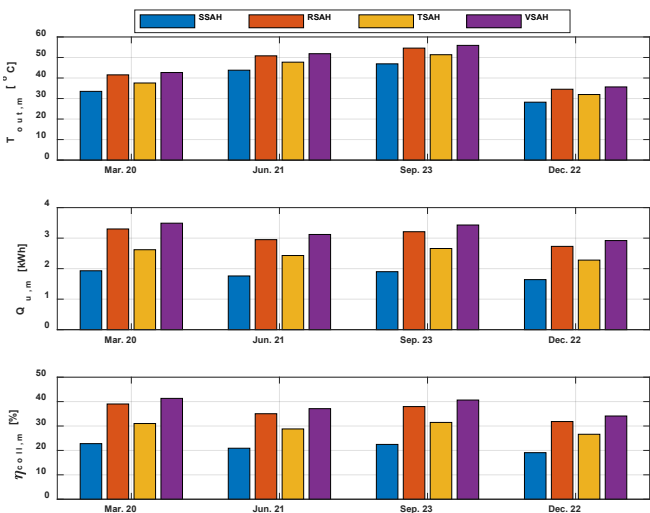
Fig. 16. Variations of useful heat gain (left) and collector efficiency (right) for different SAH absorber configurations on Dec. 22.

Figure 18 summarizes the results of the energy analysis of different mini-channel absorber collectors on a seasonal average basis. SSAH collectors have the minimum average outlet temperature ( $T_{out,m}$ ) among all collector configurations in all seasons with a maximum of 46.90 °C on Sep. 23 and a minimum value of 33.49 °C. On the other side, VSAH collectors showed the maximum average outlet temperature among all collector configurations in all seasons with a maximum of 55.90 °C on Sep. 23 (also, refer to Fig. 10). The

maximum accumulative useful heat energy is achieved by the VSAH collector. The average yearly increases in the accumulative useful heat gain ( $Q_{u,m}$ ) for VSAH collectors as compared to SSAH, RSAH and TSAH are 79.42%, 6.42% and 29.69%, respectively. This is due to the higher average daily efficiency for VSAH collectors. In addition, referring to Fig. 17, the accumulative useful heat gain from this type of collectors is the highest in all seasons, as compared to other types. The average seasonal daily efficiency range for this type of collectors is 34.10% - 41.32% as compared to 19.08% - 22.78% for the SSAH type with an average increase of 79.73%.



**Fig. 17.** Variations of accumulative useful heat energy for different SAH absorber configurations on Mar. 20, Jun. 21, Sep. 23 and Dec. 22.



**Fig. 18.** Summary of the energy analysis results.

**3.3. Exergy Performance Analysis**

The objective of the energetic analysis is to assess the available energy to the working fluid for each type of SAH under consideration. The net exergy flow to the air is

evaluated based on the useful heat gain from the collector [36].

Figure 19 shows the hourly variation of the exergy efficiency of the collector for the selected seasonal days of the year. It can be concluded from the exergetic analysis that triangular absorber geometry has the highest performance in all seasons. This second law analysis also supports the result of the energetic analysis of different configurations.

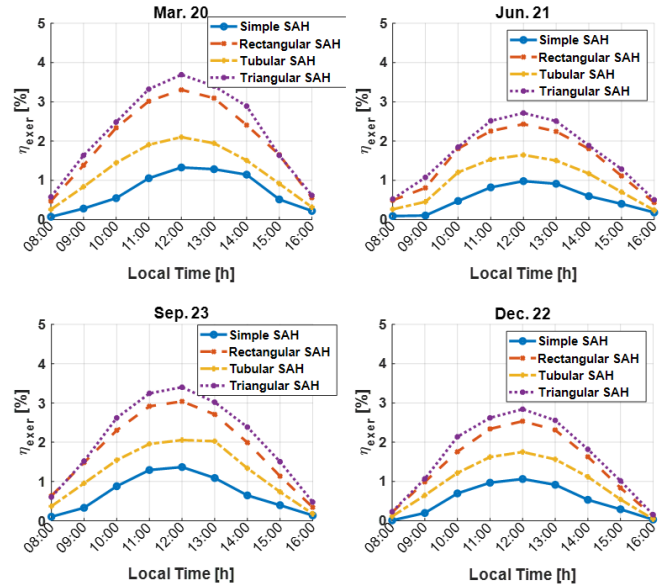


**Fig. 19.** Seasonal variations of the exergy efficiency for different SAH absorber configurations.

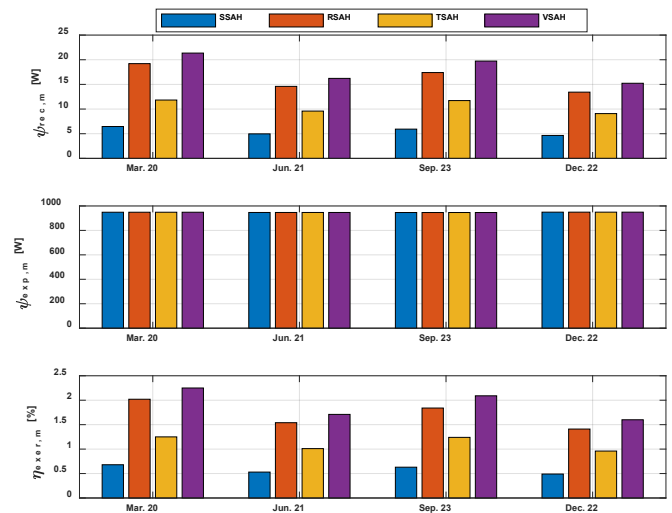


**Fig. 20.** Summary of the energy analysis results.

In the previous section, energy analysis of the SAH was conducted for performance evaluation in terms of key duty parameters such as input solar power, the useful heat gain and the collector efficiency. The collector efficiency in this case is the thermodynamic first law efficiency which represents the quantity of energy the collector can attain at certain operating conditions. On the other hand, the exergy analysis is useful to quantify available energy of different conversion process flow streams and sources of exergy destruction. The exergy efficiency (thermodynamic second law efficiency) is a qualitative tool to assess system

performance and thus maximize its conversion efficiency. This complements the energy analysis of the system to provide deeper understanding of system energy conversion behavior under various operating conditions. Figure 20 summarizes the results of the exergy analysis of different mini-channel absorber collectors on a seasonal average basis. The average expended exergy ( $\psi_{exp,m}$ ) level is almost the same for all SAH collector configurations as it depends on input solar irradiance and ambient temperature. The highest average exergy recovery ( $\psi_{rec,m}$ ) and exergy efficiency ( $\eta_{exer,m}$ ) levels are associated with VSAH collectors as compared to other collector configurations due to lower absorber temperatures and minimum heat losses. The average seasonal daily exergy efficiency range for this type of collectors is 1.60% - 2.25% as compared to 0.49% - 0.68% for the SSAH type with an average increase of 229.59%.

#### 4. Conclusions

The current work introduced a three-dimensional CFD design and comparative energetic and exergetic performance analysis of new mini-channel SAH absorber configurations at quasi-dynamic conditions, aiming at exploring the optimal design in terms of best energetic-exergetic performance parameters. The results were also compared to those for the simple absorber configuration. Hourly variations of mean temperature, pressure drop, useful heat gain, collector efficiency and exergy efficiency were obtained from the quasi-dynamic performance results. Following are the conclusions of the present study:

- Based on the fluid flow pattern, represented by the local temperature and velocity contours, triangular mini-channel absorbers were found to achieve the highest local temperatures within the mini-channels and along the flow direction, among all configurations. On the other hand, triangular mini-channel absorbers (VSAH) achieved the highest local velocities along the flow direction, among others, which resulted in a rise in the pressure drop across the collector flow on a quasi-dynamic basis.
- VSAH collectors showed the maximum average outlet temperature among all collector configurations in all seasons with a maximum of 55.90 °C on Sep. 23 but with average increases in pressure drop of 49.17% and 25.80% as compared to SSAH and RSAH collectors, respectively.
- The maximum accumulative useful heat energy is also achieved by the VSAH collector with average yearly increases of 79.42%, 6.42% and 29.69% as compared to SSAH, RSAH and TSAH, respectively. In addition, the average seasonal daily efficiency range for this type of collectors is 34.10% - 41.32% as compared to 19.08% - 22.78% for the SSAH type with an average increase of 79.73%.
- Tubular and rectangular geometrical configurations found to achieve the highest absorber mean temperatures and relatively lower outlet temperatures for all seasons, thus having lower

overall efficiency throughout the operating temperature range.

- The results of the exergetic analysis showed that the highest exergy efficiency levels are associated with VSAH collectors as compared to other collector configurations due to lower absorber temperatures and minimum heat losses. The average seasonal daily exergy efficiency range for this type of collectors is 1.60% - 2.25% as compared to 0.49% - 0.68% for the SSAH type with an average increase of 229.59%. It can be drawn that the exergy efficiency calculations support the conclusion obtained from the energy analysis for different collector configurations
- Among all mini-channel collector configurations, VSAH collectors have the potential to maximize annual energy (1183.3 kWh/m<sup>2</sup>/y) with an increase of 79.42%, as compared to annual energy collected by SSAH collectors. Accordingly, higher CO<sub>2</sub> savings could be achieved using such type of collectors.

In reference to studies on solar air heater collector configurations that depend on creating artificial roughness in the air flow path through the absorbers which adds to the complexity of the design and increase operational and initial costs, the present study introduced a new mini-channel absorber configuration (triangular) with a proven design and performance competitiveness. The comparative performance analysis of the developed design of the mini-channel SAH contributes to spreading and standardizing such efficient and cost-effective solar energy conversion technology. In addition, the proposed mini-channel absorber design has a great potential for cost-effective manufacturing techniques, e.g. though standard extrusion section processing. Further enhancements to these designs may include implementing the double pass flow pattern to increase collector yield.

#### References

- [1] M. Sarra, A. Belkaid, I. Colak, G. Boudechiche, and K. Kayisli, "Fuzzy-MPPT Controller Based Solar Shunt Active Power Filter," in 2022 11th International Conference on Renewable Energy Research and Application (ICRERA), 2022, pp. 436-440, doi: 10.1109/ICRERA55966.2022.9922873.
- [2] J. Dey, N. Mohammad, and M. Islam, "Analysis of a Microgrid having Solar System with Maximum Power Point Tracking and Battery Energy System," 10th Int. Conf. Smart Grid, icSmartGrid 2022, pp. 179-184, 2022, doi: 10.1109/icSmartGrid55722.2022.9848553.
- [3] M. Shayan, G. Najafi, and F. Ghasemzadeh, "Advanced Study of the Parabolic Trough Collector Using Aluminum (III) Oxide Seal," Int. J. Smart grid, vol. 4, no. 3, 2020, doi: 10.20508/ijsmartgrid.v4i3.108.g98.
- [4] S. Zanjani, H. Shahinzadeh, A. Oskui, W. Yaici, M. Longo, and S. Zanjani, "Performance Assessment of Heat Pump and Solar Thermal Heating with Seasonal Storage Systems for Smart Microgrid Research Center Building

- at IAUN,” 10th Int. Conf. Smart Grid, icSmartGrid 2022, no. 1, pp. 345–350, 2022, doi: 10.1109/icSmartGrid55722.2022.9848623.
- [5] J. McVeigh, “Water and Air Heating Applications,” *Sun Power*, vol. 1982, no. 97, pp. 25–64, 1983, doi: 10.1016/b978-0-08-026147-8.50009-5.
- [6] K. Ong, “Thermal performance of solar air heaters- Experimental correlation,” *Sol. Energy*, vol. 55, no. 3, pp. 209–220, 1995, doi: 10.1016/0038-092X(95)00027-O.
- [7] R. Hastings, *Solar Air Systems A Design Handbook*, 1st ed. Routledge, 2000.
- [8] H. Ghritlahre, M. Verma, J. Parihar, D. Mondloe, and S. Agrawal, “A detailed review of various types of solar air heaters performance,” *Sol. Energy*, vol. 237, pp. 173–195, 2022, doi: <https://doi.org/10.1016/j.solener.2022.03.042>.
- [9] L. Aldabbagh, F. Egelioglu, and M. Ilkan, “Single and double pass solar air heaters with wire mesh as packing bed,” *Energy*, vol. 35, no. 9, pp. 3783–3787, 2010, doi: 10.1016/j.energy.2010.05.028.
- [10] A. El-Sebaili, S. Aboul-Enein, M. Ramadan, S. Shalaby, and B. Moharram, “Thermal performance investigation of double pass-finned plate solar air heater,” *Appl. Energy*, vol. 88, no. 5, pp. 1727–1739, 2011, doi: 10.1016/j.apenergy.2010.11.017.
- [11] C. Ho, Y. Tien, and H. Chang, “Performance improvement of a double-pass V-corrugated solar air heater under recycling operation,” *Int. J. Green Energy*, vol. 13, no. 15, pp. 1547–1555, 2016, doi: 10.1080/15435075.2016.1206004.
- [12] Siddhartha, N. Sharma, and Varun, “A particle swarm optimization algorithm for optimization of thermal performance of a smooth flat plate solar air heater,” *Energy*, vol. 38, no. 1, pp. 406–413, 2012, doi: 10.1016/j.energy.2011.11.026.
- [13] A. Yadav and J. Bhagoria, “A CFD (computational fluid dynamics) based heat transfer and fluid flow analysis of a solar air heater provided with circular transverse wire rib roughness on the absorber plate,” *Energy*, vol. 55, pp. 1127–1142, 2013, doi: 10.1016/j.energy.2013.03.066.
- [14] R. Nowzari, L. Aldabbagh, and F. Egelioglu, “Single and double pass solar air heaters with partially perforated cover and packed mesh,” *Energy*, vol. 73, pp. 694–702, 2014, doi: 10.1016/j.energy.2014.06.069.
- [15] R. Nowzari, N. Mirzaei, and L. Aldabbagh, “Finding the best configuration for a solar air heater by design and analysis of experiment,” *Energy Convers. Manag.*, vol. 100, pp. 131–137, 2015, doi: 10.1016/j.enconman.2015.04.058.
- [16] A. Dissa, S. Ouoba, D. Bathiebo, and J. Kouliadiati, “A study of a solar air collector with a mixed ‘porous’ and ‘non-porous’ composite absorber,” *Sol. Energy*, vol. 129, pp. 156–174, 2016, doi: 10.1016/j.solener.2016.01.048.
- [17] S. Singh, “Performance evaluation of a novel solar air heater with arched absorber plate,” vol. 114, pp. 879–886, 2017.
- [18] I. Singh, S. Vardhan, S. Singh, and A. Singh, “Experimental and CFD analysis of solar air heater duct roughened with multiple broken transverse ribs: A comparative study,” *Sol. Energy*, vol. 188, no. April, pp. 519–532, 2019, doi: 10.1016/j.solener.2019.06.022.
- [19] S. Chamoli, R. Lu, D. Xu, and P. Yu, “Thermal performance improvement of a solar air heater fitted with winglet vortex generators,” *Sol. Energy*, vol. 159, no. November 2017, pp. 966–983, 2018, doi: 10.1016/j.solener.2017.11.046.
- [20] P. Promthaisong and S. Eiamsa-ard, “Fully developed periodic and thermal performance evaluation of a solar air heater channel with wavy-triangular ribs placed on an absorber plate,” *Int. J. Therm. Sci.*, vol. 140, no. October 2018, pp. 413–428, 2019, doi: 10.1016/j.ijthermalsci.2019.03.010.
- [21] H. Hassan, S. Abo-Elfadl, and M. El-Dosoky, “An experimental investigation of the performance of new design of solar air heater (tubular),” *Renew. Energy*, vol. 151, pp. 1055–1066, 2020, doi: 10.1016/j.renene.2019.11.112.
- [22] S. Kyaligonza and E. Cetkin, “Photovoltaic System Efficiency Enhancement with Thermal Management: Phase Changing Materials (PCM) with High Conductivity Inserts,” *Int. J. Smart grid*, vol. 5, no. 4, pp. 138–148, 2021, doi: 10.20508/ijsmartgrid.v5i4.218.g171.
- [23] P. Saravanakumar, D. Somasundaram, and M. Matheswaran, “Exergetic investigation and optimization of arc shaped rib roughened solar air heater integrated with fins and baffles,” *Appl. Therm. Eng.*, vol. 175, no. April, 2020, doi: 10.1016/j.applthermaleng.2020.115316.
- [24] S. Singh, S. Mitra, M. Kumar, and S. Suman, “Thermal performance evaluation of a solar air heater with rotating turbulators,” *Sustain. Energy Technol. Assessments*, vol. 48, p. 101647, 2021, doi: <https://doi.org/10.1016/j.seta.2021.101647>.
- [25] A. Kumar and A. Layek, “Energetic and exergetic based performance evaluation of solar air heater having winglet type roughness on absorber surface,” *Sol. Energy Mater. Sol. Cells*, vol. 230, no. November 2020, 2021, doi: 10.1016/j.solmat.2021.111147.
- [26] K. Nidhul, A. Yadav, S. Anish, and S. Kumar, “Critical review of ribbed solar air heater and performance evaluation of various V-rib configuration,” *Renew. Sustain. Energy Rev.*, vol. 142, no. March, 2021, doi: 10.1016/j.rser.2021.110871.
- [27] D. Preda, “Standardization of Solar Air Heaters,” Australia, 2017. [Online]. Available: <http://www.q-solar.com/>.
- [28] A. Razak, Z. Majid, W. Azmi, M. Ruslan, Sh. Choobchian, G. Najafi, K. Sopian, “Review on matrix thermal absorber designs for solar air collector,” *Renew.*

- Sustain. Energy Rev., vol. 64, pp. 682–693, 2016, doi: <https://doi.org/10.1016/j.rser.2016.06.015>.
- [29] H. Arunkumar, K. Vasudeva Karanth, and S. Kumar, “Review on the design modifications of a solar air heater for improvement in the thermal performance,” *Sustain. Energy Technol. Assessments*, vol. 39, p. 100685, 2020, doi: <https://doi.org/10.1016/j.seta.2020.100685>.
- [30] C. Mund, S. Rathore, and R. Sahoo, “A review of solar air collectors about various modifications for performance enhancement,” *Sol. Energy*, vol. 228, pp. 140–167, 2021, doi: <https://doi.org/10.1016/j.solener.2021.08.040>.
- [31] ANSYS Inc., “ANSYS-Fluent.” 2020, [Online]. Available: <https://www.ansys.com/products/fluids/ansys-fluent>.
- [32] European Committee for Standardization, “Thermal solar systems and components-Solar collectors-Part 2: test methods (EN 12975-2).” European Committee for Standardization, 2006.
- [33] European Commission Joint Research Centre, “Photovoltaic Geographical Information System (PVGIS),” PVGIS 5.2. [https://re.jrc.ec.europa.eu/pvg\\_tools/en/](https://re.jrc.ec.europa.eu/pvg_tools/en/).
- [34] Z. Zhang, W. Zhang, Z. Zhai, and Q. Chen, “Evaluation of various turbulence models in predicting airflow and turbulence in enclosed environments by CFD: Part 2—comparison with experimental data from literature,” *HVAC R Res.*, vol. 13, no. 6, pp. 871–886, 2007, doi: [10.1080/10789669.2007.10391460](https://doi.org/10.1080/10789669.2007.10391460).
- [35] J. Duffie and W. Beckman, *Solar Engineering of Thermal Processes*, Fourth Edi. Hoboken, New Jersey: John Wiley & Sons, Inc., 2013.
- [36] K. Altfeld, “Part 1: The Concept of Net Exergy Flow and the Modeling of Solar Air Heaters,” vol. 41, no. 2, pp. 127–132, 1988.
- [37] M. Abuşka, “Energy and exergy analysis of solar air heater having new design absorber plate with conical surface,” *Appl. Therm. Eng.*, vol. 131, pp. 115–124, 2018, doi: <https://doi.org/10.1016/j.applthermaleng.2017.11.129>.